Available online at www.sciencedirect.com
ScienceDirect
International Journal of Heat and Fluid Flow 29 (2008) 315–326
International Journal of HEAT AND FLUID FLOW
www.elsevier.com/locate/ijhff

Tomography based determination of permeability, Dupuit–Forchheimer coefficient, and interfacial heat transfer coefficient in reticulate porous ceramics

Jörg Petrasch [a], Fabian Meier [a], Hansmartin Friess [a], Aldo Steinfeld [a,b,*]

[a] Department of Mechanical and Process Engineering, ETH Zurich, 8092 Zurich, Switzerland
[b] Solar Technology Laboratory, Paul Scherrer Institute, 5232 Villigen, Switzerland

Received 3 December 2006; received in revised form 3 August 2007; accepted 6 September 2007
Available online 23 October 2007

Abstract

A computer tomography based methodology is applied to determine the transport properties of fluid flow across porous media. A 3D digital representation of a 10-ppi reticulate porous ceramic (RPC) sample was generated by X-ray tomographic scans. Structural properties such as the porosity, specific interfacial surface area, pore-size distribution, mean survival time, two-point correlation function s_2, and local geometry distribution of the RPC sample are directly extracted from the tomographic data. Reference solutions of the fluid flow governing equations are obtained for $Re = 0.2$–200 by applying finite volume direct pore-level numerical simulation (DPLS) using unstructured, body-fitted, tetrahedral mesh discretization. The permeability and the Dupuit–Forchheimer coefficient are determined from the reference solutions by DPLS, and compared to the values predicted by selected porous media flow models, namely: conduit-flow, hydraulic radius theory, drag models, mean survival time bound, s_2-bound, fibrous bed correlations, and local porosity theory-based models. DPLS is further employed to determine the interfacial heat transfer coefficient and to derive a corresponding Nu-correlation, which is compared to empirical correlations.

Keywords: Porous media; Tomography; Pore-level; Numerical simulation; Permeability; Dupuit–Forchheimer; Heat transfer coefficient

1. Introduction

Reticulate porous ceramics (RPCs) have drawn attention for applications as porous radiant burners (Howell et al., 1999; Brenner et al., 2000; Talukdar et al., 2004), as filters (Setten et al., 1999), as catalyst carriers for autothermal reformers (Dhamrat and Ellzey, 2005), and more recently as volumetric radiant absorbers in solar thermal (Fend et al., 2004) and solar thermochemical applications (Steinfeld and Palumbo, 2001; Petrasch and Steinfeld, 2005). These types of structures are advantageous as heat exchangers and catalyst supports for high temperature applications because of their high specific surface area and temperature stability. RPCs made of silicon carbide foams and coated with Rh catalyst are currently being employed for the solar steam reforming of hydrocarbons in the framework of the EU-project SOLREF (Petrasch and Steinfeld, 2005). A sample of this RPC is used in the present study; still, the methodology presented is of general applicability to porous media.

Averaging models are often applied to solve the problem of fluid flow across porous media (Whitaker, 1999; Kaviany, 1995). However, their accuracy strongly depends on the determination of the effective transport properties, such

Abbreviations: CT, computer tomography; DPLS, direct pore-level numerical simulation; FV, Finite volume method; LPT, local porosity theory; MC, Monte Carlo; RMS, root mean square; RPC, reticulate porous ceramic.

* Corresponding author. Address: Department of Mechanical and Process Engineering, ETH Zurich, 8092 Zurich, Switzerland. Tel.: +41 44 6327929; fax: +41 44 6321065.
E-mail address: aldo.steinfeld@eth.ch (A. Steinfeld).

0142-727X/$ - see front matter © 2007 Elsevier Inc. All rights reserved.
doi:10.1016/j.ijheatfluidflow.2007.09.001

Nomenclature

Latin symbols

A_0	interfacial surface area per unit solid volume (m^{-1})
A_{sf}	solid–fluid interface area (m^2)
c_0	dimensionless inverted permeability (−)
c_1	dimensionless Dupuit–Forchheimer coefficient (−)
d	diameter (m)
d_0, d_1, d_2, d_3	coefficients of Nusselt correlations (−)
d_{mm}	mean diameter of macropores (m)
d_{ms}	mean diameter of longitudinal strut pores (m)
d_{nom}	nominal pore diameter (m)
d_s	separation length scale (m)
F	Dupuit–Forchheimer coefficient (m^{-1})
$F(d)$	cumulative pore size distribution (−)
$f(d)$	pore size distribution (m^{-1})
h	interfacial heat transfer coefficient ($W/(m^2\,K)$)
K	permeability (m^2)
k_f	fluid thermal conductivity (W/(m K))
k_K	Kozeny constant
k_4, k_5	empirical constants for fibrous bed correlations
L	edge length of cell
M	set for solid matrix space
Nu	Nusselt number $Nu = hd_{nom}/k_f$
p	pressure (N/m^2)
$p(L)$	fraction of percolating cells
P	set for pore space
Pe	Peclet number $Pe = RePr$
Pr	Prandtl number $Pr = \mu c_p/k_f$
$\dot{q}'''$	volumetric heat source (W/m^3)
r	radius (m)
Re	Reynolds number $Re = \rho u_D d_{nom}/\mu$
S	set for porous medium space
s	specific surface (m^{-1})
$\hat{\mathbf{s}}$	directional vector
$s_2(r)$	two-point correlation function (−)
T	temperature (K)
T_{mf}	energy weighted mean fluid temperature (K)
T_{sf}	solid fluid interface temperature (K)
u_D	Darcean velocity (superficial velocity average) (m/s)
V	volume (m^3)
$\mathbf{x}$	point in porous medium space

Greek symbols

$\delta(\cdot)$	Dirac delta distribution
ΔT_{lm}	logarithmic mean temperature (K)
ε	porosity (–)
λ	fraction of percolating cells
μ	dynamic viscosity (kg/(m s))
$\mu_g(\varepsilon, s, L)$	local geometry distribution
$\mu_p(\varepsilon, L)$	local porosity distribution
Π_{pg}	dimensionless pressure gradient (−)
ρ	density (kg/m^3)
τ	mean survival time (s)
$\chi(\mathbf{x})$	solid-pore space indicator function
ψ	Gray value
ψ_0	solid-pore space separation gray value

as the permeability and the Dupuit–Forchheimer coefficient, obtained from the geometrical and statistical characteristics of the porous media. Kaviany (1995), Dullien (1979), and Hilfer (1996) give summaries on the methods involved. *Conduit flow* models are best suited for low porosity materials, as indicated by Dullien (1979). In contrast, models based *on flow around objects,* where the Navier–Stokes equations are solved for flow around periodic arrangements of objects, e.g. spheres or cylinders, are best suited for high porosity materials and have been applied by Kuwabara (1959), Sparrow and Loeffler (1959), and Happel and Brenner (1986). *Hydraulic radius* models are based on the concept of hydraulic radius introduced by Carman (1937). Models for *high Reynolds number flows* have been brought forward by Ergun (1952) and Ward (1964) to obtain correlations for the Dupuit–Forchheimer coefficient. *Two-point correlation bounds* for the permeability have been proposed by Berryman and Milton (1985). Torquato (1990) has introduced *permeablility bounds based on the mean survival time* τ of diffusing particles in the fluid phase. More recently application of the *local porosity theory* has been proposed by Hilfer (1996, 2002).

On the other hand, the direct pore-level numerical simulation (DPLS) of the fluid flow governing equations has become feasible with the advent of high performance computers and the ability to obtain a reasonably good geometrical representation of the porous matrix, e.g. by high resolution computer tomography (CT). Besides the underlying assumptions of the Navier–Stokes equations, no simplifications are necessary. Within the limits of the numerical truncation error (i.e., mesh refinement) and the accuracy of geometrical representation (i.e., statistical variations), DPLS approaches the exact solution. DPLS of flow in idealized unit-cells of metal-foams have been accomplished by Boomsma et al. (2003) and by Krishnan et al. (2006). CT based methods have been applied in fluid engineering applications: Pore-size distributions have been inferred from tomographic data and applied to network models by Vogel and Roth (2001). Lineal path length distributions were determined from tomographic data by Rintoul et al. (1996). Tomography based DPLS in sand-stones has been performed using Lattice-Boltzmann and finite difference methods by Manwart et al. (2002). Lattice-Boltzmann simulation of melt flow in natural partially molten

basaltic magmas has been performed by Hersum et al. (2005).

In the present paper, CT is carried out on the RPC sample to generate its 3D pore-level digital representation, from which the structural properties (e.g. porosity and specific surface area) are derived. Subsequently, finite volume based DPLS of the fluid flow is performed to obtain the "exact" reference solution and to determine the permeability and the Dupuit–Forchheimer coefficient. These are compared to the values predicted by effective property models for porous media. Finally, DPLS is further used to determine the interfacial heat transfer coefficient and a corresponding Nu-correlation; the latter is compared to experimental correlations.

2. Determination of RPC properties by CT

A 10 ppi (pores per inch) RPC sample is shown in Fig. 1. It is subjected to a polychromatic X-ray tomographic scan with a digital resolution of $30 \times 30 \times 30$ μm, using the MicroCT 80 scanner of Scanco Medical. Details of the experimental procedure have been presented in earlier work (Petrasch et al., 2007a).

A cubical $1120 \times 1120 \times 1098$ voxel subset is extracted from the CT data of the undisturbed pore-space. Solid-void segmentation using the matrix-pore separation gray value Ψ_0 is carried out according to the method of modes (Weszka, 1978). The data is further processed (Petrasch et al., 2007a) to finally obtain a continuous representation of the interface, expressed as an iso-surface:

$$\psi(\mathbf{x}) = \psi_0 \tag{1}$$

A porous medium is commonly defined as a compact set S in $\mathbb{R}^3$ consisting of two complementary sets: P representing the pore space and M representing the solid matrix. The pore space indicator function $\chi(\mathbf{x})$ is defined as

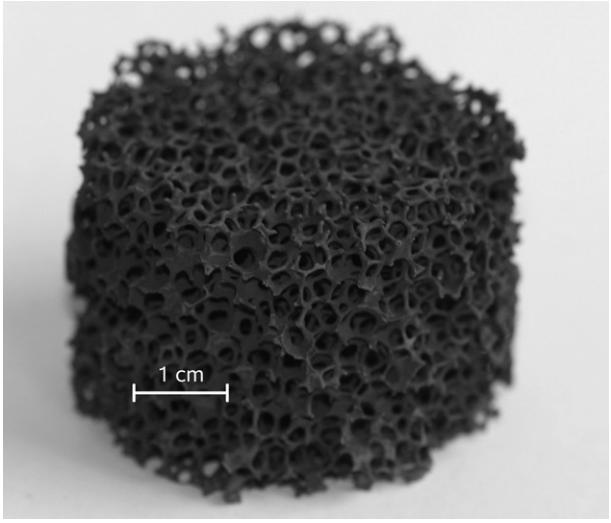

Fig. 1. Photograph of the scanned 10 ppi RPC sample.

$$\chi(\mathbf{x}) := \begin{cases} 1 & \text{if } \mathbf{x} \in P \\ 0 & \text{if } \mathbf{x} \in M \end{cases} \tag{2}$$

Based on Eqs. (1) and (2) can be rewritten as:

$$\chi(\mathbf{x}) := \begin{cases} 1 & \text{if } \psi(\mathbf{x}) < \psi_0 \\ 0 & \text{if } \psi(\mathbf{x}) \geqslant \psi_0 \end{cases} \tag{3}$$

Porosity – The porosity ε is defined as the volume fraction of the pore space relative to the total volume of the porous medium,

$$\varepsilon_{\text{tot}} = \frac{V(P)}{V(S)} = \frac{\int_s \chi(\mathbf{x}) \mathrm{d}V}{V(S)} \tag{4}$$

For a homogeneous medium, ε converges to a constant value as the size of the porous domain S is increased. For the 10 ppi RPC samples, porosity fluctuations are below 2% when $L/d_{\text{nom}} > 3.5$ (Petrasch, 2007; Petrasch et al., 2007a,b). In an analogous manner, the effective porosity ε is defined as the volume fraction of the connected pore space relative to the total volume of the porous medium. Pores that are completely enclosed by the solid matrix (i.e., not connected to the pore space) do not contribute to the fluid flow regime. They are therefore eliminated from the pore space and treated as part of the solid matrix. Thus, Eq. 4 is applied with an adjusted $\chi(\mathbf{x})$. Connectivity analysis of the CT data yields $\varepsilon_{\text{tot}} = 0.85805$ and $\varepsilon = 0.85796$. Thus, only about 0.01% of the pore volume is occupied by unconnected pores. Their influence can be neglected.

Specific surface – The specific surface s is the ratio between the interfacial area and the total volume of the porous medium.

$$s = \frac{A_{\text{sf}}(S)}{V(S)} \tag{5}$$

It can be calculated using either the Cauchy–Crofton theorem (doCarmo, 1976) or the derivative of the two-point correlation (see below). Using the latter method, the specific surface based on the raw data is $s_{\text{tot}} = 1062.08\ \text{m}^{-1}$, and the effective specific surface based on the connected pores only is $s = 1048.31\ \text{m}^{-1}$. The difference is 1.3%. Note that s accounts for structural features as small as the resolution of the tomographic scans. Smaller geometry features may be relevant for chemical/adsorption processes, but they do not influence the fluid flow since they are usually smaller than the boundary layer.

Pore size – The pore size distribution can be defined based on volume-to-surface ratios or areas of intersected pores (Murphy et al., 1977). It can also be defined based on cord length distributions (Jongerius et al., 1972), where cords are segments formed by the intersections of arbitrarily placed and oriented lines with the interface between phases.

In the present work, a pore size is associated with each point in the pore space. The pore size is defined as the diameter of the largest ball which includes this point and fits completely within the pore space (Vogel, 1997). The *opening size distribution* corresponds to this definition of

pore size. An opening is an operation of mathematical morphology, consisting of an *erosion* followed by a *dilation* using the same structuring element, thus eliminating all geometrical features smaller than the structuring element. Openings were carried out in the 3D image of the CT data, with spherical balls as structuring elements. Because of computing constraints, the $1120 \times 1120 \times 1098$ voxel dataset is re-binned to a $560 \times 560 \times 549$ voxels grid for a structuring element diameter d between 0 and 3.4 mm, and to a $373 \times 373 \times 366$ voxels grid for diameters greater than 3.4 mm. The opening size distribution $f(d)$ and the cumulative opening size distribution $F(d)$ of the RPC sample are shown in Fig. 2.

$f(d)$ exhibits two distinct maxima. The first maximum around $d = 0.18$ mm is associated with the typical diameter of the small longitudinal pores at the center of the RPC struts. The second maximum around $d = 3.2$ mm is associated with the diameter of the macroscopic pores of the RPC. The two length scales are clearly separated. The separation length scale d_s is introduced at the minimum between the two peaks; $d_s = 0.42$ mm. The mean pore diameter of the longitudinal pores d_{ms}, and the mean pore diameter of the macroscopic pores d_{mm} are defined

$$d_{ms} = \frac{\int_0^{d_s} df(d)\mathrm{d}d}{\int_0^{d_s} f(d)\mathrm{d}d} \tag{6}$$

$$d_{mm} = \frac{\int_{d_s}^{\infty} df(d)\mathrm{d}d}{\int_{d_s}^{\infty} f(d)\mathrm{d}d} \tag{7}$$

Since $f(d) = 0$ for d larger than the largest pore, integration in Eq. (7) is performed from d_s to infinity. For our RPC sample, $d_{ms} = 0.162$ mm and $d_{mm} = 3.01$ mm. The nominal pore diameter, reported by the manufacturer in pores per linear inch, is $d_{nom} = 2.54$ mm. Howell et al. (1999) found significant deviations of the measured mean pore size from the ppi values reported by manufacturers. Since d_{mm} is not readily available, all results will be normalized by d_{nom}. Note that d_{mm} is a more accurate measure and results should be scaled accordingly if available.

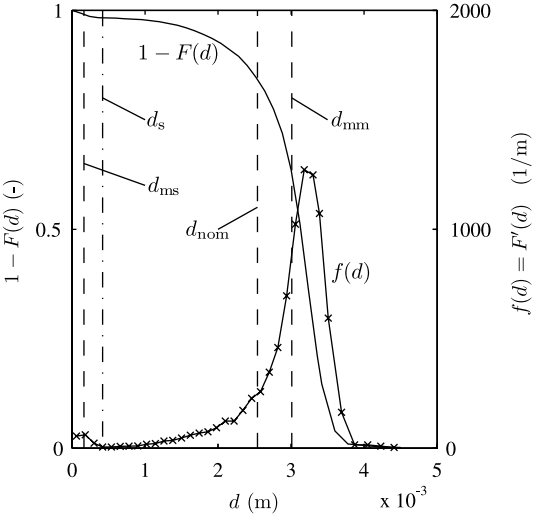

Fig. 2. Pore size distribution and cumulative pore size distribution of the scanned RPC material. d_s is the separation length scale, d_{ms} is the mean diameter of the small longitudinal pores, d_{mm} is the mean diameter of the macroscopic pores, and d_{nom} is the nominal pore size.

Survival time – The trapping rate, or its inverse, the mean survival time τ of particles in the fluid phase has been used by Rintoul et al. (1996) to obtain estimates of the permeability based on tomographic data. τ is defined as the average time a particle diffusing in the fluid phase, with a uniformly distributed source of particles and constant diffusion coefficient D, survives until it is trapped in the trapping solid phase. τD is calculated by simulating 10^6 particle trajectories based on three-dimensional random walk with Gaussian distributed step-length (Kinzelbach and Rausch, 1995). The mean step length is chosen as 1.5×10^{-5} m, hence smaller than the resolution of the tomographic scan. For our RPC sample, $\tau D = 3.73 \times 10^{-7}\,\mathrm{m}^2$. The scalar properties determined for our RPC sample using CT are listed in Table 1.

The 2-point correlation function – The s_2 correlation function and its application to porous media flow has been discussed previously (Berryman and Milton, 1985; Berryman and Blair, 1986). For homogeneous and isotropic media, it is defined as:

$$s_2(r) = \frac{\int_S \int_{4\pi} \chi(\mathbf{x})\chi(\mathbf{x} + r\hat{\mathbf{s}})\mathrm{d}\Omega\,\mathrm{d}V}{V(S)4\pi} \tag{8}$$

The most important properties of s_2 are:

$$\begin{aligned} &s_2(0) = \varepsilon \\ &\lim_{r\to\infty} s_2(r) = \varepsilon^2 \\ &\left.\frac{\mathrm{d}s_2}{\mathrm{d}r}\right|_{r=0} = -\frac{s}{4} \end{aligned} \tag{9}$$

$s_2(r)$ is inferred from tomographic data using Monte Carlo (MC) sampling. It is assumed that the porous structure is symmetrically continued in all directions, as depicted in Fig. 3. The two-point correlation calculated for the RPC sample is shown in Fig. 4.

Local porosity – Local porosity theory (LPT) consists of an approach introduced for the scale-dependent description of porous medium (Hilfer, 1991, 2002). It was applied for the prediction of its effective conductivity (Widjajakusuma et al., 2003). Porosity and specific surface area are computed for a large number N of non-overlapping cubic measurement cells with edge length L to obtain a set of

Table 1
Scalar properties of the RPC sample

Scalar property	Units	Total	Effective
ε	–	0.85805	0.85796
S	m^{-1}	1062.08	1048.31
τD	m^2	3.73×10^{-7}	
$\bar{d}$	m	3.01×10^{-3}	
$\bar{d}_s$	m	1.62×10^{-4}	
d_s	m	4.20×10^{-4}	
d_{nom}	m	2.54×10^{-3}	

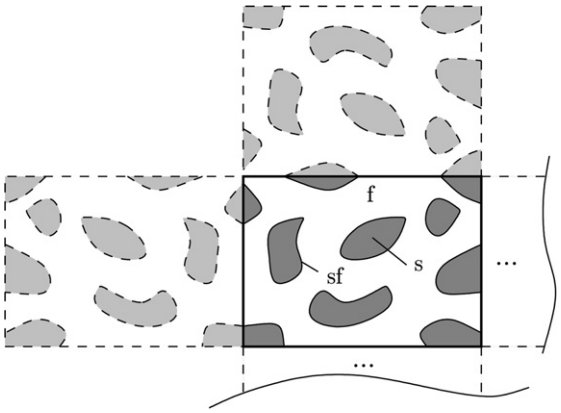

Fig. 3. Symmetric porous medium assumption for the determination of $s_2(r)$ from CT data using Monte Carlo. The medium is periodic for twice the edge length of the unit cell.

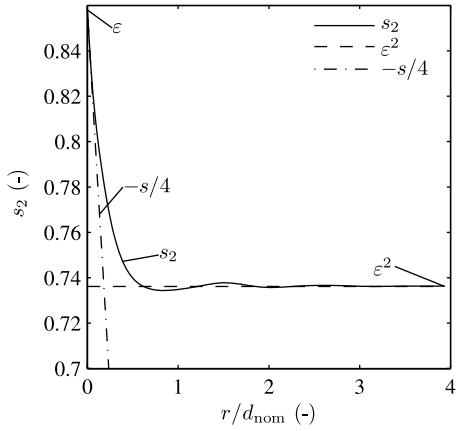

Fig. 4. Two-point correlation function of the RPC sample.

N realizations ε_i and s_i. The local porosity and local geometry distributions are then defined as:

$$\mu_{\mathrm{p}}(\varepsilon, L) = \frac{1}{N}\sum_{i=1}^{N}\delta(\varepsilon-\varepsilon_i) \tag{10}$$

$$\mu_{\mathrm{g}}(\varepsilon, s, L) = \frac{1}{N}\sum_{i=1}^{N}\delta(\varepsilon-\varepsilon_i)\delta(s-s_i) \tag{11}$$

where δ is the Dirac delta function. The connectivity of the pore space is given by the local connectivity indicator function,

$$\begin{aligned} &\Lambda(\mathbf{x}, L) = 1 \quad \text{if cell with edgelength } L \text{ percolates in all} \\ &\qquad\qquad\qquad \text{coordinate directions} \\ &\Lambda(\mathbf{x}, L) = 0 \quad \text{otherwise} \end{aligned} \tag{12}$$

A cell percolates in a coordinate direction if there exists a connected path in the pore space between two points on the opposite boundary faces perpendicular to the coordinate direction. One obtains a set of N realizations Λ_i. The local percolation probability is defined as

$$\lambda(\varepsilon, s, L) = \frac{\sum_{i=1}^{N}\Lambda_i\delta(\varepsilon-\varepsilon_i)\delta(s-s_i)}{\sum_{i=1}^{N}\delta(\varepsilon-\varepsilon_i)\delta(s-s_i)} \tag{13}$$

The total fraction of percolating cells is then

$$p(L) = \int_0^1\int_0^\infty \mu(\varepsilon, s, L)\lambda(\varepsilon, s, L)\mathrm{d}s\,\mathrm{d}\varepsilon = \frac{1}{N}\sum_{i=1}^{N}\Lambda_i \tag{14}$$

$p(L)$ computed for the RPC sample is plotted in Fig. 5 as a function of the normalized edge length. The statistical variations for large measurement cells are due to the fact that the number N of non-overlapping cells reduces as the cell size increases. The saturation length L_δ is determined as the first intersection point between $p(L)$ and $p\delta = 1-\xi$, with $\xi = 0.001$. The percolation length L_{p} is defined by:

$$\left.\frac{\mathrm{d}^2 p}{\mathrm{d}L^2}\right|_{L=L_{\mathrm{p}}} = 0 \tag{15}$$

L_{p} is found from the numerical derivative of $p(L)$ after a 7-point Savitzky–Golay smooth (MATLAB, 2005). The local

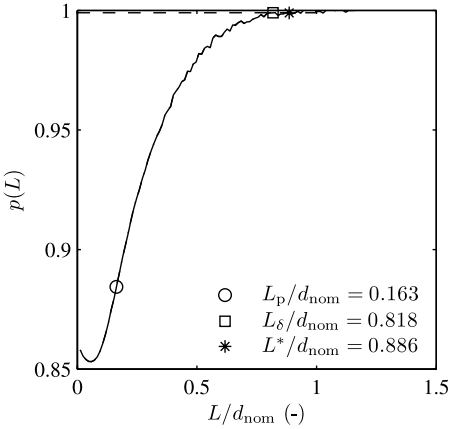

Fig. 5. Total fraction of percolation cells as a function of the normalized edge length of the measurement cell. Indicated are the percolation length L_{p}, the saturation length $L\delta$, and the length scale at which the reference permeability is exactly predicted.

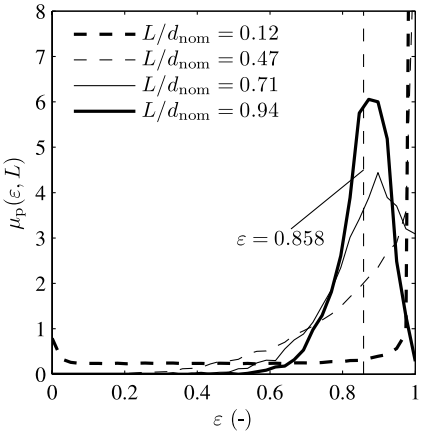

Fig. 6. Distribution of the local porosity as a function of the porosity for the RPC sample. The normalized edge length is the parameter.

porosity distributions $\mu_p(\varepsilon, L)$ for $L/d_{nom} = 0.12, 0.47, 0.71$, and 0.94 are plotted in Fig. 6 as a function of the porosity. As expected, one observes:

$$\lim_{L\to\infty} \mu_p(\varepsilon, L) = \delta(\varepsilon - \varepsilon_\infty)$$
$$\lim_{L\to 0} \mu_p(\varepsilon, L) = (1-\varepsilon)\delta(\varepsilon) + \varepsilon\delta(\varepsilon - 1) \tag{16}$$

3. Volume averaging and effective property models

Darcy's law for isotropic porous media is given by (Darcy, 1856)

$$\nabla p = -\frac{\mu}{K} u_D \tag{17}$$

The Darcean velocity, u_d, is the superficial volume average of the velocity: $u_D = \int_V u\,dV/V$, where V is a representative volume element (solid and fluid phase) of the porous medium. At higher superficial fluid velocities u_D ($Re_d > 1$), an additional quadratic term was proposed by Dupuit (1863) and Forchheimer (1901)

$$\nabla p = -\frac{\mu}{K} u_D - F\rho u_D^2 \tag{18}$$

The linear term results from viscous effects, which are predominant at low Re numbers. The quadratic term results from inertial effects. A volume averaging study by Douglas and Huiping (1992) indicates that microscopic inertial effects distort the velocity and pressure fields, which in turn lead to Forchheimer effects. Non-dimensionalization for the 1D isotropic case yields:

$$\Pi_{pg} = -c_0 - c_1 Re_d \tag{19}$$

where $\Pi_{pg} = \Delta p d^2/\mu u_D$ is the dimensionless pressure gradient, d is a characteristic length-scale (usually the average or nominal pore diameter), and Re_d is the Reynolds number based on d. Hence, c_0 is the inverse dimensionless permeability and c_1 is the dimensionless Dupuit–Forchheimer coefficient,

$$c_0 = \frac{d^2}{K}; \quad c_1 = dF \tag{20}$$

The rate of heat transferred between the porous matrix and the fluid by convection is given by:

$$\dot{q}''' = hs(T_{sf} - T_{mf}) \tag{21}$$

where h is the interfacial heat transfer coefficient, s is the specific surface area, T_{sf} is the area average of the solid–fluid interface, and T_{mf} is the mean (or bulk) mass flow-averaged fluid temperature (Incropera and DeWitt, 1996). Interfacial heat transfer coefficients are usually reported in the form of empirical Nusselt correlations, e.g.

$$Nu = d_0 + d_1 Re^{d_2} Pr^{d_3} \tag{22}$$

A number of models for the prediction of K and F as functions of the effective porosity and specific surface area are examined.

Conduit flow – According to Kaviany (1995) for a Hagen–Poiseuille flow,

$$K_C = \frac{\varepsilon d^2}{32} \tag{23}$$

Since the hydraulic radius is chosen for the pore diameter, d

$$K_C = \frac{\varepsilon^3}{2s^2} \tag{24}$$

Hydraulic radius model – This semi-heuristic model is based on the Carman–Kozeny equation (Kaviany, 1995; Dullien, 1979),

$$K_{CK} = \frac{\varepsilon^3}{k_K(1-\varepsilon)^2 A_0} = \frac{\varepsilon^3}{k_K s^2} \tag{25}$$

where A_0 is the specific surface area based on the solid volume, and k_K is the Kozeny constant, approximated as 5. A discussion of this constant can be found in Happel and Brenner (1986).

Models for fibrous beds – Empirical correlations for the permeability of fibrous beds have been proposed by Davies (Dullien, 1979)

$$K_{Da} = \frac{d_f^2}{64(1-\varepsilon)^{3/2}(1+56(1-\varepsilon)^3)} \tag{26}$$

where d_f is the fiber diameter, and by Chen (1955):

$$K_{Ch} = \frac{\pi d_f^2 \ln(k_5/(1-\varepsilon)^2)}{4k_4} \frac{\varepsilon}{(1-\varepsilon)} \tag{27}$$

where the empirical parameters $k_4 = 6.1$ and $k_5 = 0.64$. Kyan et al. (1970) derived a porosity dependent expression for the Kozeny constant,

$$k_K = \frac{(62.3N_e^2(1-\varepsilon) + 107.4)\varepsilon^3}{16\varepsilon^6(1-\varepsilon)^4}$$
$$\text{where } N_e\sqrt{\frac{2\pi}{1-\varepsilon}} - 2.5. \tag{28}$$

Drag models – The free surface model by Happel and Brenner (1986) for parallel flow along cylinders gives,

$$k_K = \frac{2\varepsilon^3}{(1-\varepsilon)\left(2\ln\left(\frac{1}{1-\varepsilon}\right) - 3 + 4(1-\varepsilon) - (1-\varepsilon)^2\right)} \tag{29}$$

For packed beds of spheres of $\varepsilon = 0.85$, $k_K = 9.6096$. For the random arrangement of cylinders of $\varepsilon = 0.85$. $k_K = 8.0506$.

Empirical model for cellular foams – Moreira et al. (2004) proposed an empirical expression for K:

$$K_{Mo} = \frac{\varepsilon^3 d_c^{0.264}}{1.36\times 10^8 (1-\varepsilon)^2} \tag{30}$$

where d_c is the cellular diameter. In the present work, $d_c = d_{nom}$.

Mean survival time – According to Torquato (1990), a rigorous bound for K is given by:

$$K_\tau \leqslant \varepsilon D\tau \tag{31}$$

where D is the diffusion coefficient and τ is the mean survival time of a fluid particle undergoing diffusion in the fluid phase. The product $D\tau$ is constant for a given porous geometry.

Two-point correlation bound – Berryman and Milton (1985) and Berryman and Blair (1986) presented a rigorous permeability bound, depending on the two-point correlation function $s_2(r)$ and the porosity ε:

$$K_{s2} \leqslant \frac{2}{3}\int_0^\infty \frac{r(s_2(r)-\varepsilon^2)}{(1-\varepsilon)^2}\,\mathrm{d}r \tag{32}$$

If the two-point correlation is approximated by two straight lines then, Eq. (32) reduces to:

$$\begin{aligned} \bar{s}_2(r) &= \varepsilon - \frac{1}{4}sr \quad \text{where } 0 < r < 4\varepsilon(1-\varepsilon)/s \\ \bar{s}_2(r) &= \varepsilon^2 \quad \text{where } 4\varepsilon(1-\varepsilon)/s \leqslant r \end{aligned} \tag{33}$$

Then, Eq. (32) reduces to:

$$k_{s2,a} \cong \frac{16}{9}\frac{\varepsilon^3}{s^2}(1-\varepsilon) \tag{34}$$

LPT – According to Hilfer (1996),

$$\int_0^\infty \int_0^1 \frac{\frac{6}{k_K}\lambda(\varepsilon,s,L)\mu(\varepsilon,s,L)}{\frac{2}{k_K}\varepsilon + 4s^2K_{LPT}}\,\mathrm{d}\varepsilon\,\mathrm{d}s = 1 \tag{35}$$

For the RPC sample, k_K is approximated as 5 and Eq. (34) is solved using $L = L_\delta$.

High Reynolds number flow – The hydraulic radius theory of Carman–Kozeny has been extended by Ergun (1952) and Macdonald et al. (1979) to give

Table 2
Model predictions for the permeability

Model	Symbol	K (m^2)	c_0 (–)	Deviation from K_{ref} (%)
DPLS	K_{ref}	1.353×10^{-7}	49.70	0.0
Conduit flow	K_C	2.873×10^{-7}	22.46	+112.3
Carman–Kozeny	K_{CK}	1.149×10^{-7}	56.15	−15.08
Fibrous beds, Davis	K_{Da}	7.388×10^{-8}	87.33	−45.40
Fibrous beds, Chen	K_{Ch}	7.897×10^{-7}	8.170	+483.7
Fibrous beds, Kyan	K_{Ky}	9.096×10^{-12}	70,930	−99.99
Cylinder, parallel flow	K_{cp}	9.379×10^{-8}	68.79	−30.67
Spheres, packed bed	K_{SP}	5.980×10^{-8}	107.9	−55.80
Cylinder, random arrangement	K_{cr}	7.138×10^{-8}	90.38	−47.24
Empirical, cellular foams	K_{Mo}	4.7558×10^{-8}	135.7	−64.85
Two-point correlation bound	K_{s2}	7.650×10^{-7}	8.433	+465.4
Two-point correlation, approximation	$K_{s2,a}$	1.445×10^{-7}	44.65	+6.79
Mean survival time bound	$K_D\tau$	3.185×10^{-7}	20.26	+135.4
LPT, L_p	$K_{LPT}(L_p)$	–	–	–
LPT, L_δ	$K_{LPT}(L_\delta)$	1.484×10^{-7}	43.47	+9.68

Table 3
Model predictions for the Dupuit–Forchheimer coefficient

Model	Symbol	F (m^{-1})	c_1(–)	Deviation from F_{ref} (%)
DPLS	F_{ref}	444.02	1.128	0.0
Ergun/Macdonald	F_E	497.98	1.265	+12.15
Ward	F_W	1495.2	3.798	+236.74
Empirical, cellular foams	F_{Mo}	964.4	2.450	+117.2

$$F_E = 1.8\frac{1-\varepsilon}{\varepsilon^3}\frac{1}{d} \tag{36}$$

with $d = \frac{6}{A_0}$.

Ward (1964) recommends:

$$F_w = \frac{0.550}{\sqrt{K}} \tag{37}$$

Moreira et al. (2004) give an empirical correlation for F in cellular foams:

$$F_{Mo} = \frac{1.8\times10^4(1-\varepsilon)}{\varepsilon^3 d_c^{-0.24}} \tag{38}$$

All results are compiled in Tables 2 and 3. Table 2 lists the predicted values of the permeability and of c_0 ($c_0 = d^2/K$) by the averaging models. Also listed is the "exact" reference value K_{ref} obtained by DPLS (see next section) and the relative difference with the predicted values by the averaging models. Table 3 lists the predicted values of the Dupuit–Forchheimer coefficient and of c_1 ($c_1 = dF$). Also listed is the "exact" reference value F_{ref} obtained by DPLS (see next section) and the relative difference with the predicted values by the averaging models.

4. Direct pore-level numerical simulation (DPLS)

DPLS of fluid flow across the RPC sample is performed. An in-house mesh generator for unstructured body-fitted grids was developed for the present CFD study. This was necessary because of the inability of commercial software products to use directly the pore indicator function $\chi(x)$ and the excessively long computing times consumed for the large meshes ($>10^7$ volume elements) that are required with the complex RPC geometry. Our mesh generator initially covers the domain by a tetrahedral mesh where all elements have the same shape. In a second step, the mesh is iteratively refined close to the solid–fluid interface. The refining algorithm is directly based on the solid-pore indicator function, similar to the methodology described by Bey (1995). In a final step, the mesh is fitted to the interface by means of "rounding" and "cutting". "Rounding" refers to projecting vertices to the interface if they are sufficiently close to it, and "cutting" refers to replacing volume elements intersected by the interface with an adequate arrangement of one or more smaller elements.

The ANSYS-CFX (ANSYS-CFX, 2006) finite volume CFD code is used to solve the 3D incompressible

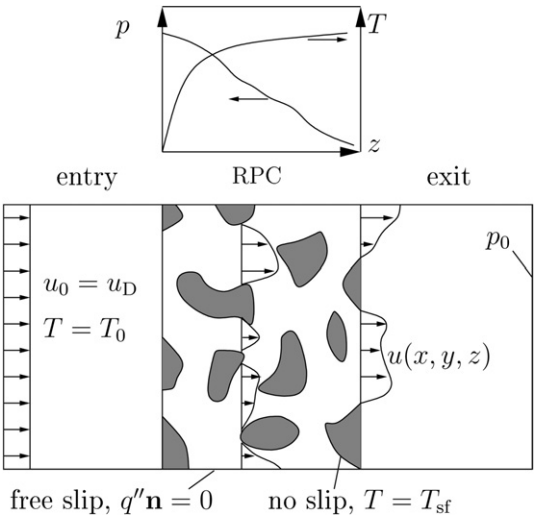

Fig. 7. Schematic of CFD domain and its boundary conditions.

continuity and Navier–Stokes equations in the pore-space. The computational domain consists of a square duct that is made up of an undisturbed inlet and exit region and an intermediate test section containing the RPC's 3D mesh representation. A uniform inlet velocity and temperature profile $u_0 = u_D$ and $T = T_0$, and an outlet pressure p_0 are given as boundary conditions. Further, the walls of the duct have free-slip boundary condition, and the solid fluid interface has a no-slip boundary condition. The boundary conditions in the computational domain are depicted in Fig. 7.

A small $60 \times 60 \times 60$ voxels subset of the tomographic dataset (subset A) is used to determine the necessary degree of mesh refinement. Grids with a representative mesh length scale in the range 16.07–128.6 μm were generated and fluid flows at Reynolds numbers of 1 and 100 were simulated on each of the grids. A representative mesh length scale of 64.3 μm ($=0.0253 d_{nom}$) is chosen for all further calculations. The relative difference between the pressure drop for the simulation of flow in subset A using the representative grid and that using the finest grid (with a representative mesh length scale of 16.07 μm) was 1.3% at $Re = 1$ and 3.1% at $Re = 100$. Preliminary calculations are carried out in a $240 \times 240 \times 240$ voxel ($=7.2 \times 7.2 \times 7.2$ mm^3 $=2.835 \times 2.835 \times 2.835 d_{nom}^3$) subset of the tomographic data (subset B) using the representative length scale determined in subset A. Fig. 8 shows a 2D projection of the grid for subset B.

Determination of K and *F* – A representative $800 \times 800 \times 280$ voxel($= 24 \times 24 \times 8.4$ mm^3 $= 9.45 \times 9.45 \times 3.31 d_{nom}^3$) subset of the tomographic data (subset C) is used to generate a grid with a mesh length scale of 0.0253 d_{nom}, resulting in $1.24 \cdot 10^7$ tetrahedral elements. Periodicity is not assumed. This elemental geometry is used to minimize boundary effects since preliminary simulations showed that the entry length is small (smaller than 0.1 d_{nom} or 0.254 mm) compared to the sample thickness of 8.4 mm.

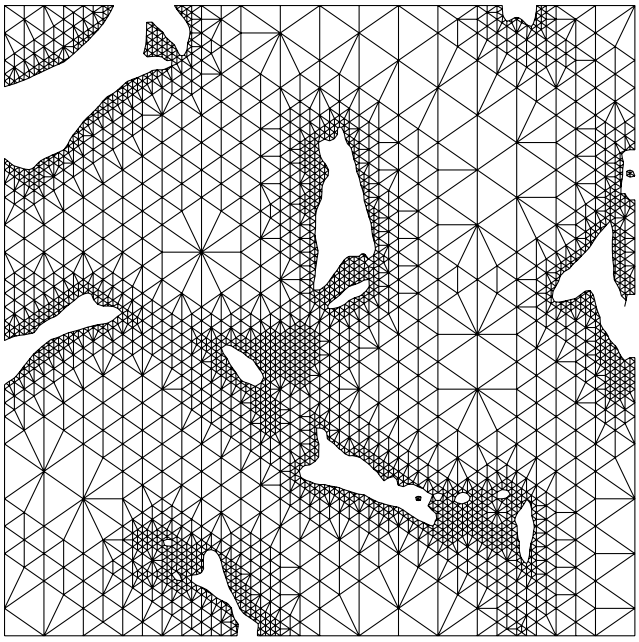

Fig. 8. 2D projection of subset B fluid phase tetrahedral grid generated by the in-house mesh generator.

The non-dimensional pressure profile $\frac{p d_{nom}}{\mu u_D}$ averaged over the pore space in cross-sections perpendicular to the main flow direction, is plotted in Fig. 9 for flows at $Re = 0.2$–20. Deviations from the ideal linear pressure profile are due to statistical fluctuations in the local porous medium properties. The slope is equal to the non-dimensional pressure gradient Π_{pg}. As expected, the curves collapse to a single curve for the limit of low Reynolds numbers, i.e. in the Darcy regime. Hence, in the Darcy regime, the slope equals $-c_0$ ($c_0 = d^2/K$).

Flow calculations are carried out for $Re = 0.2$, 0.4, 1, 2, 4, 10, 20, 40, 100, and 200. A hybrid interpolation scheme is used for the finite volume flux calculations. The mean dimensionless pressure gradient $\Delta p d_{nom}^2 / \mu u_D$ is plotted in Fig. 10 as a function of the Reynolds number. As expected, it is almost constant up to $Re = 2$ (Darcy regime), while the influence of the Dupuit–Forchheimer term becomes predominant at high Reynolds numbers.

The dimensionless parameters c_0 and c_1 obtained via least square fitting of Eq. (19), are $c_{0,ref} = 49.70$ and $c_{1,ref} = 1.128$. The RMS of the fit is 1.8%. Thus, the "exact" reference values[1] of the permeability and the Dupuit–Forchheimer coefficient are $K_{ref} = 1.353 \times 10^{-7}$ m^2 and $F_{ref} = 444.02$.

The best model predictions are also indicated in Fig. 10. In spite of its relative simplicity, the Carman–Kozeny model (Eq. 25) estimates K with a relative error of −15.08%. LPT using the saturation length scale (Eq. 35)

[1] Exact within the limits of the numerical truncation error (i.e., mesh refinement) and the accuracy of geometrical representation (i.e., statistical variations).

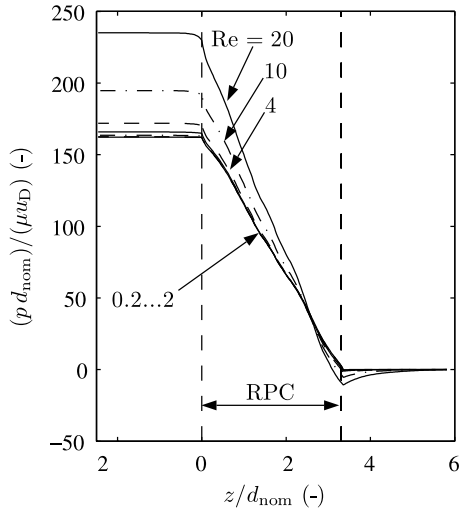

Fig. 9. Non-dimensional average pressure profile in the fluid phase along main flow direction across the RPC sample, calculated by DPLS. The parameter is the flow Reynolds number: $Re = 0.2$–20.

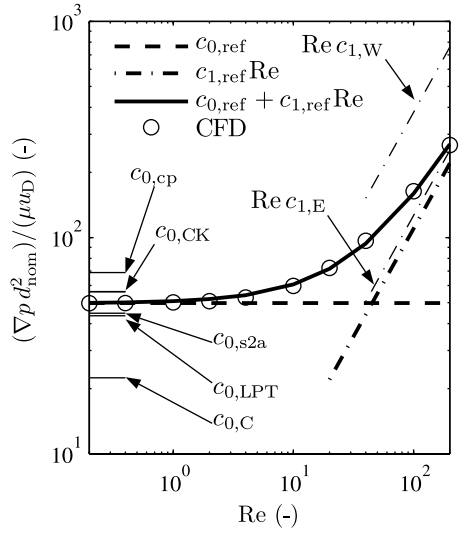

Fig. 10. Dimensionless pressure gradient as a function of the Reynolds number, calculated by DPLS. Indicated are the best model predictions of c_0 and c_1 using the porous medium properties determined by CT.

estimates K with +9.68% relative error, but it reproduces K_{ref} for $L^*/d_{\mathrm{nom}} = 0.886$. The two-point correlation bound (Eq. 32) fails to give a reasonably estimate of c_0, while its simpler approximation (Eq. 34) predicts K within 6.79% of K_{ref}. The models based on cylinders in parallel flow and on the conduit flow model predict K with a relative error of −30.67% and +112.3%, respectively. Finally the empirical model by Moreira (eq.) underestimates K by 64%. F is well predicted by the Ergun/Macdonald model (Eq. 36) with an error 12.15%, whereas the value predicted by Ward model (Eq. 37) results in a relative error of +236.74% and the model by Moreira (Eq. 38) results in a relative error of +117.2%.

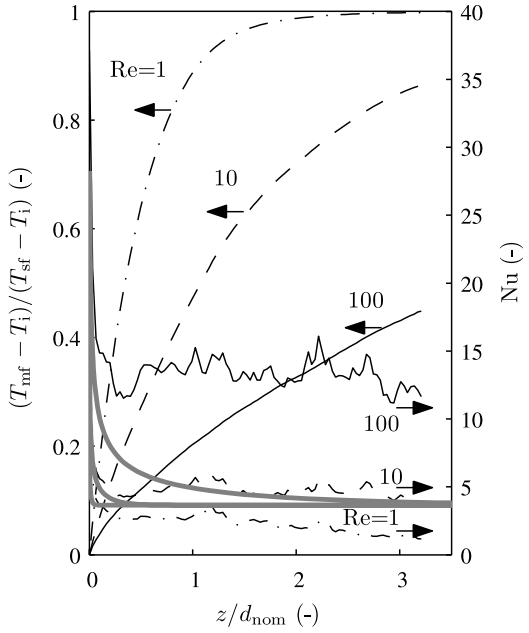

Fig. 11. Dimensionless temperature profile and local Nusselt number as a function of the dimensionless distance from the RPC inlet, calculated by DPLS at $Pr = 1$. The parameter is the Reynolds number: $Re = 1$, 10, and 100. Also plotted is the local Nusselt number for laminar flow in circular tubes at $Pr = 1$, $Re = 1$, 10, and 100 (gray lines).

Determination of the interfacial heat transfer coefficient- The same sample and mesh as for the fluid flow calculations are used for the heat transfer calculation. In addition to the boundary conditions imposed on the fluid flow, the fluid inlet temperature is specified, the temperature of the porous medium solid–fluid interface is specified as constant, and the square duct walls are assumed adiabatic. Simulations are carried out for $0.2 < Re < 200$ and $Pr = 0.1$, 0.5, 1, and 10. Viscous dissipation is neglected.

The local heat transfer coefficient averaged over the surface area between locations z and Δz is defined as:

$$h\Delta T_{\mathrm{lm}}(T_{\mathrm{sf}}, T_{\mathrm{mf}}(z), T_{\mathrm{mf}}(z+\Delta z)) = \int_z^{1+\Delta z} \dot{q}''\,\mathrm{d}A_{\mathrm{sf}} \qquad (39)$$

The local Nusselt number and dimensionless fluid temperature $\frac{T_{\mathrm{mf}}-T_i}{T_{\mathrm{sf}}-T_i}$ are plotted in Fig. 11 as a function of the dimensionless distance z/d_{nom} for flows at $Re = 1$, 10 and 100, and for $Pr = 1$. As the fluid enters the porous medium, the local Nusselt number quickly drops to an almost constant value. Fluctuations are due to the inherently statistical nature of the porous geometry. Also plotted is the local Nusselt number for laminar flow in a circular tube with constant wall temperature and diameter d_{nom} at $Re = 1$, 10 and 100, and for $Pr = 1$ (Kays and Crawford, 1993). Whereas the mean Nusselt number depends on the Reynolds number for RPCs, it is independent of Re for tubes ($\mathrm{Nu} = 3.66$).

The mean Nusselt number is shown as a function of Re in Fig. 12, for various values of the Prandtl number. The parameters of Eq. (22), obtained via least square fitting,

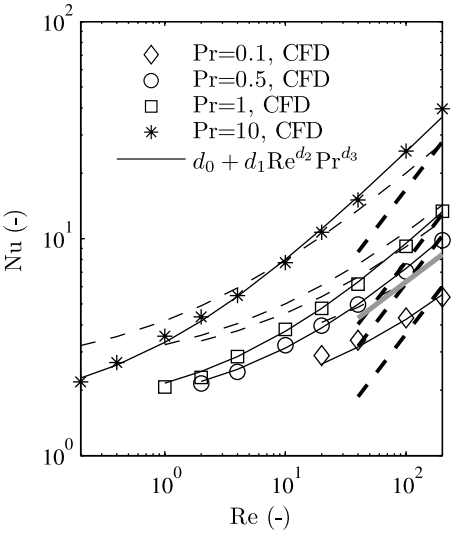

Fig. 12. Mean Nusselt number and fitted correlation as a function of Reynolds number, calculated by DPLS. The parameter is the Prandtl number. Also plotted are the empirical Nu correlations by Buck (2000) at $Pr = 0.1$, 0.5, 1, 10 (thick, dashed lines), by Younis and Vikanta (1992) at $Pr = 0.7$ (solid gray line), and for packed beds at $Pr = 0.1$, 0.5, 1, 10 (dashed lines).

are $d_0 = 1.5590$, $d_1 = 0.5954$, $d_2 = 0.5626$, $d_3 = 0.4720$. The constant d_0 is necessary to determine the Nusselt number at small Peclet numbers. For a single sphere d_0, it approaches 2. Deviation from this value is due to the porous microgeometry and the choice of the reference length scale, d_{nom}. The RMS of the fit is 3.9%. For comparison, the empirical Nusselt correlation for a 20 ppi Al_2O_3 ceramic foam with an effective porosity of 80%, derived by Buck (2000) for $150 < Re < 500$, is:

$$Nu_{d_\mathrm{h}} = 0.2942 Re_{d_\mathrm{h}}^{0.7277} Pr^{1/3} \tag{40}$$

where $d_\mathrm{h} = 4\varepsilon/s$. Note that this correlation uses the hydraulic diameter as the reference length scale. The empirical Nusselt correlation for a 20 ppi cordierite foam, derived by Younis and Viskanta (1992) for an air flow at $65 < Re < 457$ is:

$$Nu = 0.243 Re^{0.42}/(s \cdot d_{\mathrm{nom}}) \tag{41}$$

For comparison, results of an empirical Nusselt correlation for packed beds given in Schlünder et al. (1984) are also shown in Fig. 12:

$$\begin{aligned} Nu_{\mathrm{bed}} &= (1 + 1.5(1-\varepsilon)) Nu_{\mathrm{sphere}} \\ Nu_{\mathrm{sphere}} &= 2 + \sqrt{Nu_{\mathrm{lam}}^2 + Nu_{\mathrm{turb}}^2} \\ Nu_{\mathrm{lam}} &= 0.664^3 \sqrt{Pr}\sqrt{Re} \\ Nu_{\mathrm{turb}} &= \frac{0.037 Re^{0.8} Pr}{1 + 2.443 Re^{-0.1}(Pr^{2/3} - 1)} \end{aligned} \tag{42}$$

Note that the original correlation is given for the volumetric heat transfer coefficient and has to be normalized by $s \times d_{\mathrm{nom}}$ to arrive at comparable results. Given the fact that the ceramic foams are from different manufacturers, have different nominal pore diameters, and the ranges of Re overlap only partly, the agreement between the DPLS and the experimental results is reasonably good.

5. Conclusions

Tomography based determination of effective porous media properties has been performed for reticulate porous ceramics (RPCs). The structural properties of RPCs were extracted from 3D tomographic data obtained with $30 \times 30 \times 30$ μm^3 digital resolution scans. It included, for example, an effective porosity of 0.86 and an effective geometrical specific surface area of 1048 m^{-1}. The pore size distribution, determined from the opening size distribution, exhibited two distinct peaks that were identified with the length scale of the small longitudinal pores central to the strut material ($\bar{d}_\mathrm{s} = 0.162$ mm) and with the length scale of the macroscopic pores ($\bar{d} = 3.01$ mm), respectively. The fraction of unconnected pores was found to be negligible, while the mean macroscopic pore size was found to be larger than the one specified by the manufacturer. The two-point correlation function was determined using MC sampling. Local geometry distribution and total percolation probability, required for the LPT models, yielded percolation and saturation lengths of 0.414 and 2.08 mm, respectively.

A finite volume direct pore-level numerical simulation (DPLS) was applied for $Re = 0.2$–200 using an unstructured tetrahedral mesh. The DPLS solution, which can be considered as approaching the exact solution within the limits of the numerical truncation error (i.e., mesh refinement) and the accuracy of geometrical representation (i.e., statistical variations), yielded a permeability of $1.353 \cdot 10^{-7}$ m^2. This reference value was compared to predictions from structural properties by applying selected porous media flow models. For example, the classical Carman–Kozeny equation and the LPT predict the permeability within 15% and 9.7% of the reference value, respectively. In contrast, the rigorous bounds from the mean survival time overestimates the permeability by 135%. The simple approximation of the two-point correlation bound provides the most accurate estimation, with a relative error of 6.8%. A reference value for the Dupuit–Forchheimer coefficient of 444 m^{-1} was determined by DPLS for high Reynolds numbers, while the Ergun/Macdonald model predicts it with a relative error of 12%.

Finally, a constant interface temperature Nusselt correlation for the convective heat transfer coefficient was derived based on DPLS for $Re = 0.2$–200, $Pr = 0.1$–10 and $Pe > 1$. The Nusselt numbers obtained are within the range of the experimentally based correlations for similar materials. The local Nusselt number is almost constant (with statistical fluctuations) everywhere in the medium except at the short entry region.

Tomography based determination of the effective flow properties of porous media by direct pore-level solution of the fluid flow governing equations has been demon-

strated for RPCs. The methodology allows for detailed analysis of heat and fluid flow at the pore level and is not constrained to parameter ranges imposed by purely experimental determination. In the current study, results are limited to the RPC structure considered. The method is applicable to any porous structure that can be resolved tomographically. Morphological operations such as dilation and erosion can be used to obtain effective transport parameters as a function of porosity.

Acknowledgements

This work has been carried out in the framework of the SOLREF Project, funded by the European Commission under contract No. SES6-CT-2004-502829 SOLREF. We thank P. Wyss and R. Stämpfli from EMPA for the experimental support during the tomographic measurements.

References

Ansys Inc., 2006. ANSYS-CFX.

Berryman, J.G., Blair, S.C., 1986. Use of digital image analysis to estimate fluid permeability of porous materials: application of two-point correlation functions. J. Appl. Phys. 60, 1930–1938.

Berryman, J.G., Milton, G.W., 1985. Normalization constraints for variational bound on fluid permeability. J. Chem. Phys. 83 (2), 754–759.

Bey, J., 1995. Tetrahedral grid refinement. Computing 55, 355–378.

Boomsma, K., Poulikakos, D., Ventikos, Y., 2003. Simulations of flow through open cell metal foams using an idealized periodic cell structure. Int. J. Heat Fluid Flow 24, 825–834.

Brenner, G., Pickenäcker, K., Pickenäcker, O., Trimis, D., Wawrzinek, K., Weber, T., 2000. Numerical and experimental investigation of matrix-stabilized methane/air combustion in porous inert media. Combust. Flame 123, 201–213.

Buck, R. 2000. Massenstrom-Instabilitäten bei volumetrischen Receiver-Reaktoren.

Carman, P.C., 1937. The determination of the specific surface area of powder I. J. Soc. Chem. Ind. 57, 225–234.

Chen, C.Y., 1955. Filtration of aerosols by fibrous media. Chem. Rev. 55, 595.

Darcy, H., 1856. Les Fontaines Publiques de la ville de Dijon. Dalmont, Paris.

doCarmo, M.P., 1976. Differential Geometry of Curves and Surfaces. Prentice-Hall.

Douglas, R., Huiping, M., 1992. On the derivation of the Forchheimer equation by means of the averaging theorem. Transport in Porous Media 7, 255–264.

Dullien, F., 1979. Porous Media Fluid Transport and Pore Structure. Academic Press.

Dupuit, J., 1863. Etudes theoretiques et practiques sur le mouvement des eaux. Dunond, Paris.

Ergun, S., 1952. Fluid flow through packed column. Chem. Eng. Prog. 48, 89–94.

Fend, T., Hoffschmidt, B., Pitz-Paal, R., Reutter, O., Rietbrock, P., 2004. Porous materials as open volumetric solar receivers: experimental determination of thermophysical and heat transfer properties. Energy 29 (5–6), 823–833.

Forchheimer, P., 1901. Wasserbewegung durch den Boden. Z. Ver. Deutsch. Ing. 45, 1782–1788.

Happel, J., Brenner, H., 1986. Low Reynolds Number Hydrodynamics. Martinus Nijhoff Publishers.

Hersum, T., Hilpert, M., Marsh, B., 2005. Permeability and melt flow in simulated and natural partially molten basaltic magmas. Earth Planetary Sci. Lett. 237.

Hilfer, R., 1991. Geometric and dielectric characterization of porous media. Phys. Rev. B 44 (1), 60–75.

Hilfer, R., 1996. Transport and relaxation phenomena in porous media. In: Prigogine, I., Rice, A. (Eds.), Adv. Chem. Phys. XCII. John Wiley & Sons.

Hilfer, R., 2002. Review on scale dependent characterization of the microstructure of porous media. Transport in Porous Media 46, 373–390.

Howell, J., Hall, M., Ellzey, J., 1999. Combustion of hydrocarbon fuels within porous inert media. Prog. Energy Combust. Sci. 22 (2), 121–145.

Incropera, F., DeWitt, D., 1996. Introduction to Heat Transfer. John Wiley & Sons, Inc., New York, Chichester, Brisbane, Toronto, Singapore.

Jongerius, A., Schoonderbeek, D., Jager, A., 1972. The application of the quantimet 720 in soil micromorphometry. The Microscope 20, 243–254.

Kaviany, M., 1995. Principles of Heat Transfer in Porous Media. Springer-Verlag, New York, Berlin, Heidelberg.

Kays, W., Crawford, M., 1993. Convective heat and mass transfer. McGraw-Hill, New York.

Kinzelbach, W., Rausch, R., 1995. Grundwassermodellierung. Borntraeger, Stuttgart.

Krishnan, S., Murthy, J.Y., Garimella, S.V., 2006. Direct Simulation of transport in open-cell metal foam. ASME J. Heat Transfer, 128.

Kuwabara, S., 1959. The forces experienced by randomly distributed parallel circular cylinders or spheres in a viscous flow at small Reynolds numbers. J. Phys. Soc. Japan 14 (4), 527–532.

Kyan, C.P., Wasan, D.T., Kintner, R.C., 1970. Flow of single phase fluids through fibrous beds. Ind. Eng. Chem. Fundam. 9 (7), 596.

Macdonald, I.F., El-Sayed, M.S., Mow, K., Dullien, F.A.L., 1979. Flow through porous media – Ergun equation revisited. Ind. Eng. Chem. Fundam. 18, 199–208.

Manwart, C., Aaltosalmi, U., Koponen, A., Hilfer, R., Timonen, J., 2002. Lattice-Boltzmann and finite-difference simulation for the permeability for three-dimensional porous media. Phys. Rev. E 66, 16702-1-8.

The MathWorks, 2005. MATLAB.

Murphy, C.P., Bullock, P., Biswell, K.J., 1977. The measurement and characterisation of voids in soil thin sections by image analysis Part II. Applications. J. Soil Sci. 28, 509–518.

Moreira, E., Innocentini, M., Coury, V., 2004. Permeability of ceramic foams to compressible and incompressible flow. J. Eur. Ceram Soc. 24, 3209–3218.

Petrasch, J., 2007. Multi-scale Analyses of Reactive Flow in Porous Media, Doctoral dissertation, ETH Zurich Diss. ETH No. 17192.

Petrasch, J., Steinfeld, A., 2005. Solar steam-reforming of hydrocarbons – thermodynamic analysis and process simulation. In: 18th International ECOS-Conference, June 20–22, Trondheim, Norway.

Petrasch, J., Schrader, B., Wyss, P., Steinfeld, A., 2007a. Tomography-based determination of the effective thermal conductivity of reticulate porous ceramics. ASME Journal of Heat Transfer, in review.

Petrasch, J., Wyss, P., Steinfeld, A., 2007b. Tomography-based Monte Carlo determination of radiative properties of reticulate porous ceramics. J. Quant. Spectrosc. Radiat. Transfer 105, 180–197.

Dhamrat, R., Ellzey, J., 2005. Numerical and experimental study of the conversion of methane to hydrogen in a porous media reactor. Combust. Flame 144 (4), 698–709.

Rintoul, M.D., Torquato, S., Yeong, C., Keane, D.T., Erramilli, S., Jun, Y.N., Dabbs, D.M., Aksay, I.A., 1996. Structure and transport properties of porous magnetic gel via x-ray microtomography. Phys. Rev. E 54 (3), 2663–2669.

van Setten, B.A., Bremmer, J., Jelles, S.J., Makkee, M., Moulijn, J.A., 1999. Ceramic foam as a potential molten salt oxidation catalyst support in the removal of soot from diesel exhaust gas. Catal. Today 53 (4), 613–621.

Schlünder, E. et al. (Eds.), 1984. VDI-Wärmeatlas - Berechnungsblätter für den Wärmeübergang. VDI-Verlag, Düsseldorf.

Sparrow, E.M., Loeffler, A.L., 1959. Longitudinal laminar flow between cylinders arranged in regular array. Am. Inst. Chem. Engrs. J. 5, 325–330.

Steinfeld, A., Palumbo, R., 2001. Solar Thermochemical Process Technology in Encyclopedia of Physical Science and Technology. In: Meyers, R.A. (Ed.). Academic Press.

Talukdar, P., Mishra, S.C., Trimis, D., Durst, F., 2004. Heat transfer characteristics of a porous radiant burner under the influence of a 2-D radiation field. J. Quant. Spectrosc. Radiat. Transfer 84, 527–537.

Torquato, S., 1990. Relationship between permeability and diffusion-controlled trapping constant of porous media. Phys. Rev. Lett. 64 (22), 2644–2646.

Vogel, H.J., 1997. Morphological determination of pore connectivity as a function of pore size using serial sections. Eur. J. Soil Sci. 48, 365–377.

Vogel, H.J., Roth, K., 2001. Quantitative morphology and network representation of soil pore structure. Adv. Water Resour. 24, 233–242.

Ward, J.C., 1964. Turbulent flow in porous media. J. Hyd. Div. ASCE 90, 1–12.

Weszka, J., 1978. A survey of threshold selection techniques. Comput. Graph. Image Process. 7, 259–265.

Whitaker, S., 1999. The Method of Volume Averaging. Kluwer, Dordrecht.

Widjajakusuma, J., Biswal, B., Hilfer, R., 2003. Quantitative comparison of mean field mixing laws for conductivity and dielectric constants of porous media. Physica A 318, 319–333.

Younis, L.B., Viskanta, R., 1992. Experimental determination of the volumetric heat transfer coefficient between stream of air and ceramic foam. Int. J. Heat Mass Transfer 36 (6), 1425–1434.